AUTOMATIC GENERATION OF BOUNDARY CONDITIONS USING DEMONS NON-RIGID IMAGE REGISTRATION FOR USE IN 3D MODALITY-INDEPENDENT ELASTOGRAPHY

By

Thomas S. Pheiffer

Thesis

Submitted to the Faculty of the

Graduate School of Vanderbilt University

in partial fulfillment of the requirements

for the degree of

MASTER OF SCIENCE

in

Biomedical Engineering

May, 2010

Nashville, Tennessee

Approved:

Professor Michael I. Miga

Professor Robert L. Galloway

ACKNOWLEDGEMENTS

I would like to thank my advisor Dr. Michael Miga for his guidance and Dr. Jao Ou for all of his advice and development of the algorithm which forms the basis for this work. I am also grateful to the rest of the members of the BML and SNARL labs for their friendship and support, particularly Rowena Ong in sharing her data and Dr. Amber Simpson for her advice. I would also like to thank the Vanderbilt Medical Center CT department for the scans of our phantoms, as well as Dr. Thomas Yankeelov and Dr. John Boone (University of California-Davis Medical Center, Dept. of Radiology) for the human breast MR and CT data sets, respectively.

TABLE OF CONTENTS

LIST OF TABLES

Table Page

LIST OF FIGURES

Figure Page

LIST OF ABBREVIATIONS

Abbreviation	Full Name
1. TPS	Thin-plate spline
2. MIE	Modality-independent elastography
3. FEM	Finite element method
4. BC	Boundary conditions
5. SCP	Symmetric closest point
6. TRE	Target registration error
7. PDE	Partial differential equation
8. MR	Magnetic resonance
9. CT	Computed tomography
10. w/v	Weight per volume

CHAPTER I

INTRODUCTION

1.1 Motivation

Breast cancer is second only to lung cancer in cancer-induced mortality among women. The American Cancer Society estimated that in 2009, over 194,000 new cases of invasive breast cancer would be diagnosed, in addition to over 62,000 cases of in situ breast cancer, and an estimated 40,000 deaths from the disease that year. Additional statistics underscore the importance of early initiation of treatment, as the five-year relative survival rates for women diagnosed with breast cancer are only approximately 27% for advanced distant-stage disease, but are as high as 98% for early localized disease (ACS 2009). In addition, tumor size has been directly correlated to prognosis of 5- to 10-year survival, and has significant implications for long-term survival (Michaelson, Silverstein et al. 2002; Warwick, Tabar et al. 2004). Early detection is therefore both an inherently desirable goal and one which presents demands for more sensitive detection techniques.

Breast cancer lesions have traditionally been detected clinically by palpation and imaging modalities such as X-ray mammography. Palpation allows for the qualitative contrast of diseased tissue from normal tissue by recognizing that cancerous lesions are generally firmer to the touch than normal tissue. This allows for identification of regions that may require biopsy for histological examination. However, palpation suffers from having a short depth of detection into the tissue, and is subjective in nature.

Mammography, while being the standard technique for breast screening, has been shown to have questionable reliability when used in isolation (Keith, Oleszczuk et al. 2002).

An alternative imaging methodology that, like palpation, utilizes the mechanical properties of tissue is known as elastography. Elastography employs a combination of image processing and measurements of the physical deformation of the tissue to create a representation of the mechanical strength of structures inside the breast (Bilgen 1999; Doyley, Meaney et al. 2000). The overall principle behind elastography for use in breast cancer imaging is that regional changes in tissue architecture resulting from the manifestation of disease result in detectable changes in mechanical properties. It is widely recognized in the medical community that most breast cancers are much firmer to the touch than the surrounding soft tissue. The biological basis for this effect is due to changes in tissue composition, such as varied expression of collagen and greater numbers of fibroblasts (Burns-Cox, Avery et al. 2001; Lee, Sodek et al. 2007). The exploitation of a contrast mechanism based on elastic properties may have considerable potential as means for characterization of disease states.

Several kinds of elastography exist, such as ultrasound elastography (USE) and magnetic resonance elastography (MRE) which have already shown promise in diagnosing solid lesions in breast tissue and other physiological locations. The first introduction of USE demonstrated that images from A-line ultrasound could provide axial strain estimates (Ophir, Cespedes et al. 1991). Elastography has also been applied within the MR imaging domain whereby motion-sensitized gradient sequences were used to visualize and quantify strain wave propagation in media (Muthupillai, Lomas et al. 1995). A relatively new method known as modality-independent elastography (MIE) has

recently shown potential for supplementing other imaging modalities such as MR and CT for detection of solid tumors in soft tissue (Miga 2003).

MIE has the benefit of being flexible with regard to its inputs, and unlike USE and MRE, it is not reliant on a particular imaging modality. MIE involves imaging a tissue of interest before and after compression, and then applying a finite element (FE) soft-tissue model within a nonlinear optimization framework in order to determine the elastic properties of the tissue. A requirement of the MIE method is that appropriate boundary conditions be designated for use in the biomechanical model. Generation of accurate boundary conditions is problematic because the breast is a non-rigid structure, which invalidates the use of standard rigid registration techniques. Techniques which have addressed this issue in the past have required a significant amount of user interaction. The goal of this work is to develop and validate a method of generating boundary conditions automatically by registering breast surfaces before and after mechanical loading. This method may have potential not only in MIE, but also in other applications requiring registration of breast surfaces.

1.2 Previous Work

The methods used for registering breast images generally fall into one of two broad categories: 1) feature-based methods or 2) intensity-based methods (Guo, Sivaramakrishna et al. 2006). Feature-based methods utilize geometric information from the images, such as from an FE mesh of the breast structure, to register two breast images. Intensity-based methods instead directly use the intensity values of the image voxels, and optionally some geometric information, to register the two images.

The previous gold standard in generating boundary conditions for MIE has been feature-based registration methods (Ou, Ong et al. 2008). Conventionally this entails employing point correspondence methods facilitated by attached fiducials and assisted by thin-plate spline (TPS) interpolation (Goshtasby 1988) to create the boundary conditions that non-rigidly maps the pre-deformed breast surface to the post-deformed breast surface. This registration process requires the tedious task of applying and subsequently localizing numerous surface markers within the image space, determining point correspondence, creating a thin-plate spline interpolation, and finally calculating a set of Dirichlet boundary conditions for use in the MIE method. Initial attempts to reduce the complexity and level of user interaction have focused on the use of two energy minimization techniques (Ong, Ou et al. 2010). These techniques relied upon partial differential equation (PDE) solutions of Laplace's equation,

$$\nabla \cdot (-\sigma \nabla \Phi) = 0, \tag{1}$$

or the diffusion equation,

$$\frac{\partial \Phi}{\partial x} = \nabla \cdot (\alpha \nabla \Phi), \tag{2}$$

across the surface of the breast geometry in the pre- and post-deformed states. Like-valued isocontours from the solutions on each surface (i.e. pre-deformed, and post-deformed) act as 'virtual' fiducials to assist in correspondence using a symmetric closest point approach (Papademetris, Sinusas et al. 2002). Dirichlet boundary conditions are generated after the assigned correspondence is determined and this completes the required input for the MIE algorithm. The primary difference between the two methodologies is the boundary condition requirement and subsequently the required degree of user interaction. For the Laplacian method, Dirichlet boundary conditions were

required to be assigned to two distinct regions of the mesh surface (points along the chest wall, and nipple were assigned potential values of 1 and 0, respectively, with unity conductivity). For the diffusion method, only one distinct region need be designated (in this case an initial condition of zero potential was supplied, with a unity Dirichlet condition assigned at the nipple). While the results presented by Ong *et al.* (2010) indicated better performance via the Laplacian method, the diffusion method did not require the difficult task of assigning a boundary condition to the chest wall in both pre- and post-deformed mesh domains. These methods, as well as the TPS method, will be compared to the intensity-based approach in this paper.

While the above PDE-based methods represented an improvement in automation over the TPS method for generating boundary conditions for the MIE algorithm, the ideal boundary condition method would be both fully automated and require no fiducials. This study presents an approach for automatically generating boundary conditions through the use of a popular non-rigid image registration algorithm called demons diffusion. The demons algorithm was used to perform image matching of pre- and post-deformation images and tested against a controlled *in silico* simulation with known boundary conditions. The generated boundary conditions were also used to perform an MIE elasticity reconstruction to evaluate its effectiveness in determining the elasticity contrast of a previously characterized system. The simulation study was followed by two phantom experiments to further stress the abilities of this new approach.

CHAPTER II

METHODOLOGY

2.1 MIE Workflow

As described in previous work, the MIE algorithm is comprised of three major components: 1) a biomechanical FE model of soft-tissue deformation based on material properties, 2) a similarity metric with which to compare images, and 3) an optimization routine to update the material properties in the model (Miga, Rothney et al. 2005).

The process of generating an elasticity reconstruction begins with the acquisition of an image of the breast. A mechanical load is then applied to the breast, and the breast is imaged again. These pre- and post-deformation images comprise the primary input to the MIE algorithm, and are referred to as the source and target images, respectively. The breast boundary is then segmented in the pre-deformed source image and its surface geometry is extracted using the marching cubes algorithm, which allows a finite element mesh to be created from the surface information. The mesh is partitioned into 'regions' to which elasticity properties are assigned, which defines the resolution of the elastographic reconstruction. It is then necessary to designate the loading/boundary conditions for the FE model. The ability of the biomechanical model to accurately deform the mesh of the breast tissue is dependent on these boundary conditions. The boundary condition step in the MIE workflow is highlighted in Figure 1.

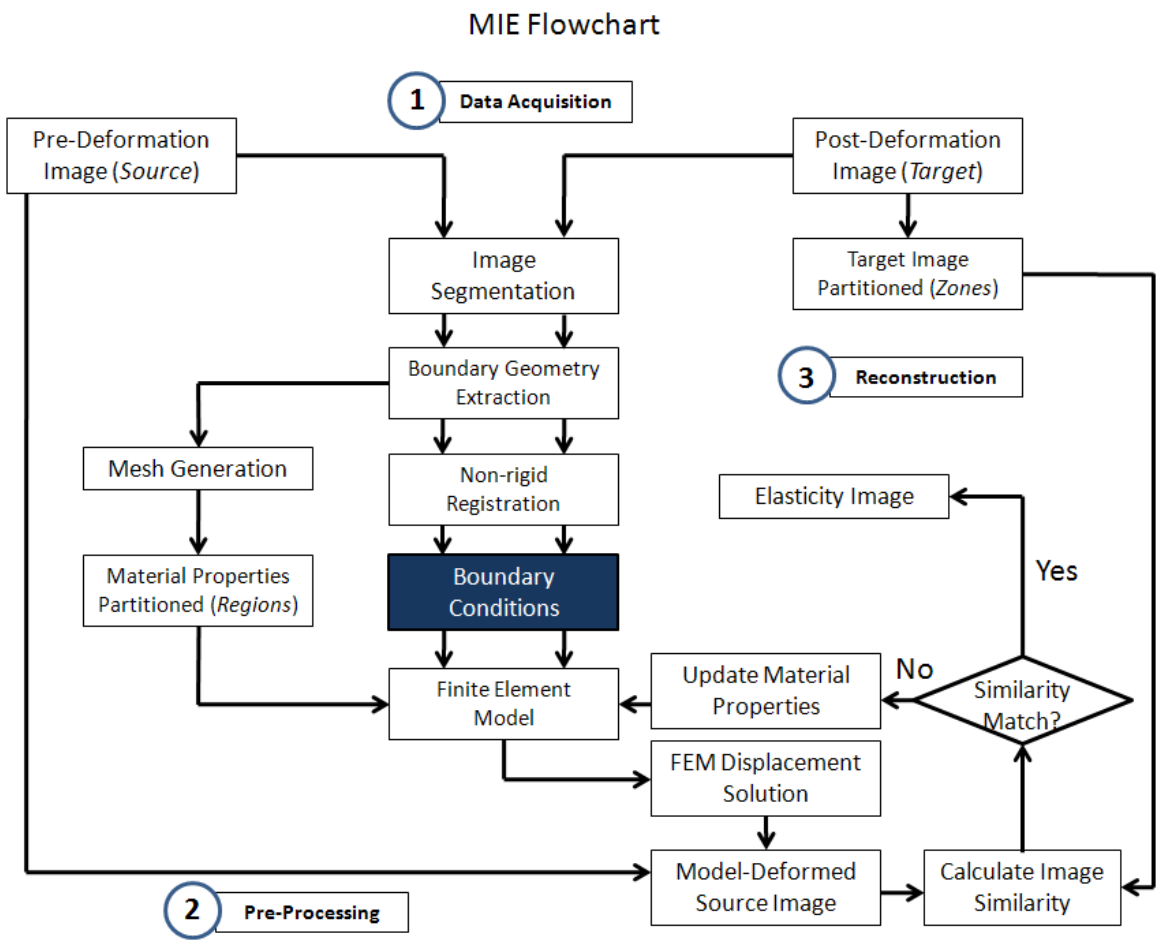

Figure 1. Overview of the MIE protocol. The boundary condition task is seen to be in a central location and has a critical impact on the final reconstruction.

Once boundary conditions have been designated, the model is run and the FEM displacement solution for all the nodes in the mesh is obtained. The displacements are then used to deform the original pre-deformation image, which is then compared with the known post-deformation image to generate an image similarity measurement. A non-linear optimization framework is used to update the material properties of the mesh until the similarity metric is within tolerance, at which point the elasticity reconstruction image is produced.

2.2 Automatic Generation of Boundary Conditions

The demons registration algorithm utilizes a diffusion model in which the object boundaries in one image are characterized as semi-permeable membranes, and the other image is allowed to diffuse through these membranes (Thirion 1998). Following the formulation of Ibanez, *et al*.(Ibanez, Schroeder et al. 2005),

$$\mathrm{D(X)} \cdot \nabla f(\mathrm{X}) = -\big(\mathrm{m(X)} - \mathrm{f(X)}\big) \tag{3}$$

where f(X) is the fixed target image, m(X) is the source image being deformed for the registration, and D(X) is the displacement field mapping the source to the target image through an instantaneous optical flow. The algorithm used in this work was based on the Insight Toolkit (Yoo, Ackerman et al. 2002), which reformulated Equation 3 to an algorithmic iterative form as follows:

$$\mathrm{D^N(X)} = \mathrm{D^{N\text{-}1}(X)} - \frac{\left(\mathrm{m}\left(\mathrm{X}+\mathrm{D^{N\text{-}1}(X)}\right)-\mathrm{f(X)}\right)\nabla \mathrm{f(X)}}{\|\nabla \mathrm{f}\|^2+\left(\mathrm{m}\left(\mathrm{X}+\mathrm{D^{N\text{-}1}(X)}\right)-\mathrm{f(X)}\right)^2} \tag{4}$$

The displacement field obtained from Equation 4 is smoothed with a Gaussian filter between each iteration in order to enforce elastic-like behavior. This aspect of the algorithm's implementation made it appropriate for modeling the boundary conditions of a system being deformed within the confines of an elastic model.

The registration produces displacements at the centroid of every voxel. The displacement vectors are then interpolated onto the nodal coordinates of the FE mesh using a cubic 3D interpolation. The displacements which are assigned to boundary nodes are thus designated as the Type I boundary conditions for the elastic model.

2.3 Simulations

In order to evaluate the demons method of generating boundary conditions for MIE as described above, a controlled experiment was conducted by obtaining a CT and an MR image volume of human breast tissue and registering them to target images created by simulated mechanical loads.

Two image sets (CT and MR) of normal tumor-free human breast tissue were obtained from the UC-Davis Department of Radiology and the Vanderbilt University Institute of Imaging Science, respectively, for use in this work. The surface of each breast image was segmented from the surrounding structures with ANALYZE 8.1 (Mayo Clinic, Rochester, MN) and the resulting segmentation was used to create a 3D FE mesh using a tetrahedral mesh generation algorithm (Sullivan, Charron et al. 1997). For both the CT set and the MR set, a 2-cm spherical tumor was synthetically implanted in the center of the respective mesh and assigned an elasticity value six times higher than the surrounding material, which is consistent with breast cancer elasticity contrasts in the literature (Krouskop, Wheeler et al. 1998). This contrast ratio of 6:1 was thus considered to be the goal for reconstruction in both cases. The location of the tumor in each mesh is visualized in Figure 2.

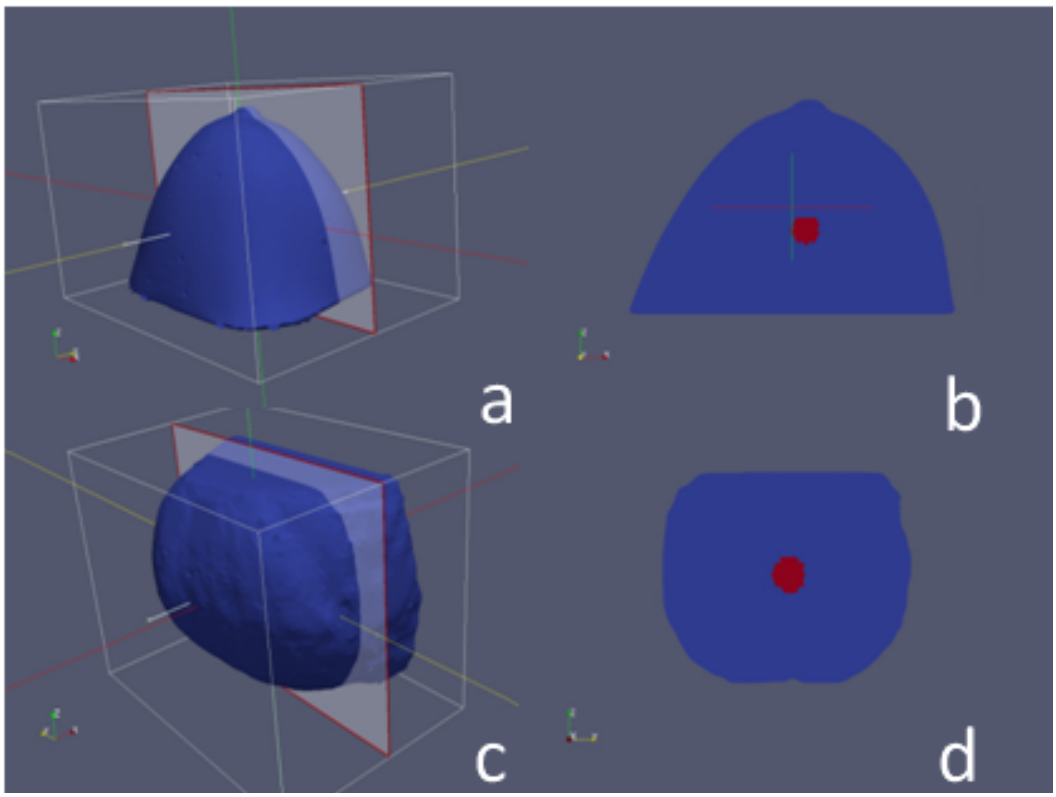

Figure 2. Source CT mesh (a) with cross-section showing tumor-to-normal elasticity contrast (b), and source MR mesh (c) with cross-section showing similar contrast (d).

Each finite element mesh was then deformed by applying a depression to one side of the breast. The displacements predicted by the model were then used to deform the CT and MR source images to provide simulated target images. Using the pre- and post-deformed image volume sets, the demons registration could be executed and compared to the known displacements responsible for the simulated breast deformations. In addition, the surface displacements could be used to test the accuracy and fidelity of the 3D MIE reconstructions conducted with demons-based boundary conditions.

2.4 Phantom Experiment 1

After demonstrating the efficacy of the demons method in the highly controlled *in silico* simulation study, the next step was to apply the same tests to real-world data with

realistic amounts of noise and uncertainty. To this end, breast phantom images were acquired to evaluate the ability of the demons method to produce accurate boundary conditions when compared to the current gold standard method.

As described by Ong *et al.* (2010), the breast phantom used in this study (hereafter referred to as Phantom 1) was created from an 8% w/v solution of polyvinyl alcohol (Flinn Scientific, Batavia, IL). The gel was frozen in a breast-shaped mold at -37°C for 16 hours and then allowed to thaw at room temperature to produce a tissue-mimicking breast phantom. To provide intrinsic fiducial markers, thirty-four 1-mm stainless steel beads were distributed over the phantom directly under its surface. It should be noted that, except for the beads, there was little to provide intensity heterogeneity within this phantom. A mechanical load was applied to the phantom in a custom-built acrylic chamber via a neoprene sphygmomanometer air bladder (W.A. Baum, Copiague, NY) positioned on the side of the phantom. This compression device was constructed so that an adjustable wall could be positioned to hold the phantom in place, while on the opposite side the air bladder was located approximately at the midpoint of the height of the phantom.

The phantom was subjected to three levels of compression by inflation of the air bladder: no compression, inflation with 50% of the maximum bladder pressure, and full inflation of the bladder. At each state of compression, CT images were acquired with dimensions 512 x 512 x 174, and 0.54 x 0.54 x 1 mm voxel size. The images were then segmented and triangular meshes were created from the surface geometry of the phantom. The uncompressed mesh was composed of 8,127 nodes, the 50% compression mesh was composed of 6,777 nodes, and the 100% compression mesh was composed of

8,260 nodes. From the meshes, the fiducial bead centroid positions were localized and then used in a TPS interpolation to provide the gold standard boundary conditions for two scenarios: 1) deforming from the uncompressed state to the 50% compression state, and 2) deforming from the uncompressed state to the 100% compression state. In generating the TPS boundary conditions, 33 of the beads were used in calculating the interpolation, while the last fiducial was used to evaluate the target registration error (TRE). In an effort to evaluate the error over the entire surface, the TPS registration was conducted 34 times, each time using a different fiducial for the TRE calculation. The final TRE for the TPS gold standard was the average of these repetitions. The demons method was then used independently to generate boundary conditions mapping from the pre- to the post-deformed surface of the breast phantom for the two scenarios, and compared to the control TPS result, as well as previous semi-automated methods (Laplace equation and diffusion methods). The registration in both scenarios utilized 120,000 iterations and a Gaussian smoothing kernel standard deviation of 1.5.

2.5 Phantom Experiment 2

Following the evaluation of the performance of the demons method in generating boundary conditions in the above phantom study, a second phantom experiment was designed to test the performance of demons-based boundary conditions in the context of a full MIE reconstruction. Two more phantoms (hereafter referred to as Phantom 2 and Phantom 3) were constructed of polyvinyl alcohol cryogel (PVA-C) to test the accuracy of the reconstruction when validated with material testing data.

As described by Ou, the two new phantoms were created with a 7% w/v suspension of hydrolyzed polyvinyl alcohol powder heated to 80°C, which was then incorporated with 10% glycerol (Fisher Scientific, Pittsburgh, PA) by volume (Ou 2008). Due to the nature of the polymerization of the gel, sequential freeze-thaw cycles (FTCs) achieve varying levels of stiffening elasticity. A FTC in this study was defined as bringing the gel down to -37°C over the course of 12 hours and then allowing it to return to room temperature over the next 12 hours.

The two phantoms were constructed by first mixing the components described above. To test the ability of the MIE algorithm, there needed to be a detectable difference in the elasticity between the phantom tumor and the rest of the phantom breast. In order to make the tumor stiffer than the normal tissue, the bulk of the phantom was subjected to one FTC, while the tumor underwent two FTCs. The tumor was made in a 25-mm diameter spherical mold for its first FTC, and was then suspended with very thin plastic wires approximately in the center of the mold used to simulate the shape of a pendant breast. While the FTCs produce elasticity contrast between the tumor gel and normal gel, it does not produce an appreciable CT image contrast between the two materials to enable the MIE similarity metric to detect differences in the deformed images. In order to introduce more contrast into the images, a small amount of radiopaque contrast was initially added to the tumor mixture in the form of a 6% v/v quantity of barium sulfate suspension (Lafayette Pharmaceuticals, Lafayette, IN). Prior to the second FTC, a 3% v/v barium sulfate mixture was injected into the bulk breast gel in a few random streams to improve the overall image texture. The second FTC then proceeded and the wires suspending the tumor were removed to produce the final anthropomorphic breast

phantom containing a stiff tumor. Similar to the first phantom study, polytetrafluoroethylene spherical beads (McMaster-Carr, Atlanta, GA) with a 1.6-mm diameter were distributed just under the surface of the phantoms in order to facilitate a TPS interpolation to act as the gold standard boundary conditions. Phantom 2 received 35 beads, while Phantom 3 received 32 beads. The TRE for the TPS registration was calculated using a 'leave-one-out' strategy similar to the approach described in the first phantom experiment.

In order to evaluate the performance of MIE when using the demons-based boundary conditions, validation was needed for the material property contrast between the tumor and normal gel. To achieve this, independent mechanical tests were performed on samples of the two gel elasticity constituents of the phantom. A sample from each gel (tumor and normal) was set aside for this testing during fabrication. Each was poured into standard 24-well polystyrene cell culture plates (Corning Inc. Corning, NY) and subjected to its respective number of FTCs. This process resulted in cylindrical gel samples with diameter and height both about 15 mm, which could then be subjected to compression testing using an ElectroForce 3100 material tester (Bose, Eden Prairie, MN). The instrument was programmed to provide fixed displacements to the cryogels when the samples were mounted on a platform over a 22.5 N load cell. Each sample was subjected to five cycles of a load rate of 0.15 mm/s and then held for 300 s for strains of 2, 5, 10, and 15% in compliance with small deformation theory. Average elastic modulus values for the two gels were obtained from the slope of the stress-strain curves of the steady-state loading phases.

The two phantoms were constructed with tumors located at varying distances from the surface being compressed. The maximum diameter at the base of both phantoms was approximately 105 mm. The Phantom 2 tumor was approximately 12 mm below the surface, while the Phantom 3 tumor was approximately 26 mm below the surface. The phantoms were imaged in the previously described air bladder chamber using a CT scanner (Philips Medical, Bothell, WA). The Phantom 2 CT images (pre- and post-deformation) were reconstructed with dimensions of 512x512x143 and voxel spacing of 0.27 x 0.27 x 0.8 mm, while the Phantom 3 CT images were reconstructed with dimensions of 512x512x139 and voxel spacing of 0.26 x 0.26 x 0.8 mm.

The pre-deformed source image volumes were segmented from the compression chamber and their surface information was used to create tetrahedral meshes. The Phantom 2 mesh was constructed of 30,900 nodes and 166,509 elements, while the Phantom 3 mesh was constructed of 33,930 nodes and 183,609 elements. The TPS boundary conditions were generated using the implanted beads as control points for a thin-plate spline interpolation between the pre- and post-deformation surfaces for each phantom set. The PDE-based and demons methods were then utilized to independently generate boundary conditions for the two phantoms. The demons registration was set to run for 30,000 iterations for these sets, with a Gaussian smoothing kernel standard deviation of 1.5.

The accuracy of the demons-based boundary conditions could then be evaluated by comparing the gold standard TRE of the TPS method, the TRE of the PDE-based methods, and the TRE of the points when used in the demons method. The appropriateness of demons-based boundary conditions was then tested by employing

them in a MIE reconstruction comparing elastic modulus values to independent measurements. To constrain the problem, only two regions of material properties were designated in the mesh: the tumor and the bulk normal gel. *A priori* knowledge of the location of the tumor was also used by segmenting the tumor margins from the normal gel beforehand in order to assign the material types to their corresponding elements in the FE model. The results of the MIE reconstruction using demons-based boundary conditions were also compared to the results of the reconstruction when using TPS boundary conditions, and those derived from the PDE methods. The Poisson's ratio used in the model for both experiments was 0.485 to approximate an incompressible tissue-mimicking material.

CHAPTER III

RESULTS

3.1 Simulations

The CT and MR image source images were acquired and then deformed with the set of known boundary conditions as shown below in Figure 3.

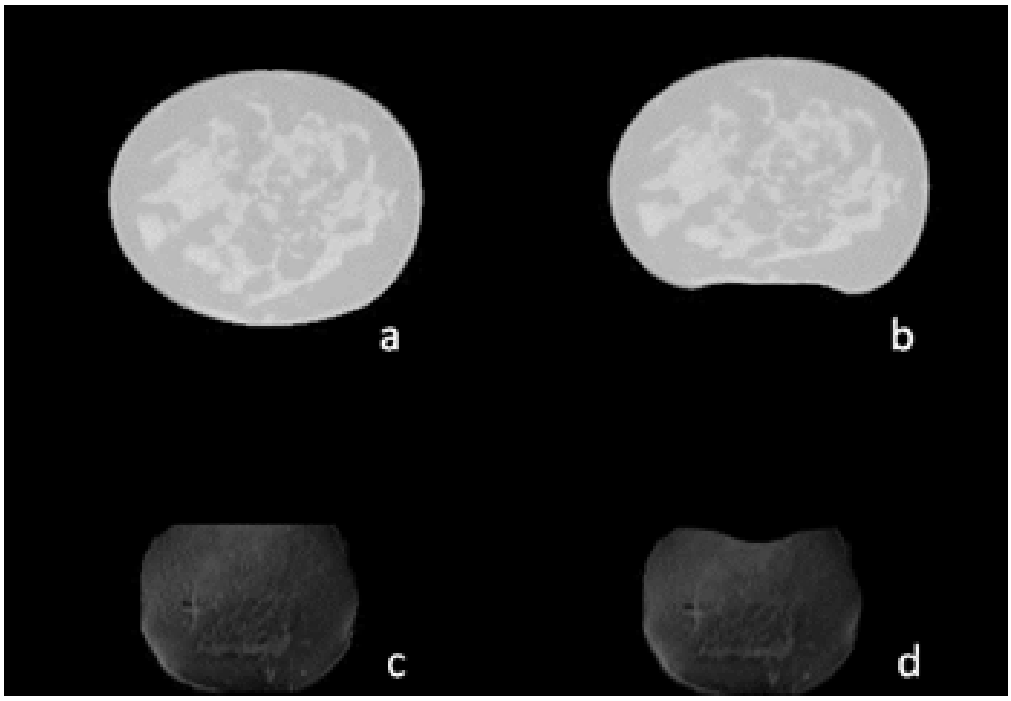

Figure 3. Representative slices from the two data sets used for the simulations. Slice (a) shows the CT image in its pre-deformed state, and (b) shows the CT image in its post-deformed state. Slice (c) shows the MR image in its pre-deformed state, and (d) is the MR image in its post-deformed state.

Figures 3a and 3b show an axial slice from the pre-deformed (left) and post-deformed (right) CT image volume, respectively. Figures 3c and 3d show a pre-deformed (left) and post-deformed (right) slice from the MR image volume, respectively.

The deformations applied in both cases were approximately Gaussian in distribution across the depressions as shown in Figure 4 below. The maximum displacement experienced by the CT set was approximately 13 mm and was applied to the side of the source CT mesh (Figure 4a) to result in the target post-deformed mesh (Figure 4b) which was used to create the simulated target image for this experiment. The MR mesh was similarly deformed by applying an approximately 12 mm depression to the top of the source MR mesh (Figure 4c) to result in the simulated MR mesh (Figure 4d).

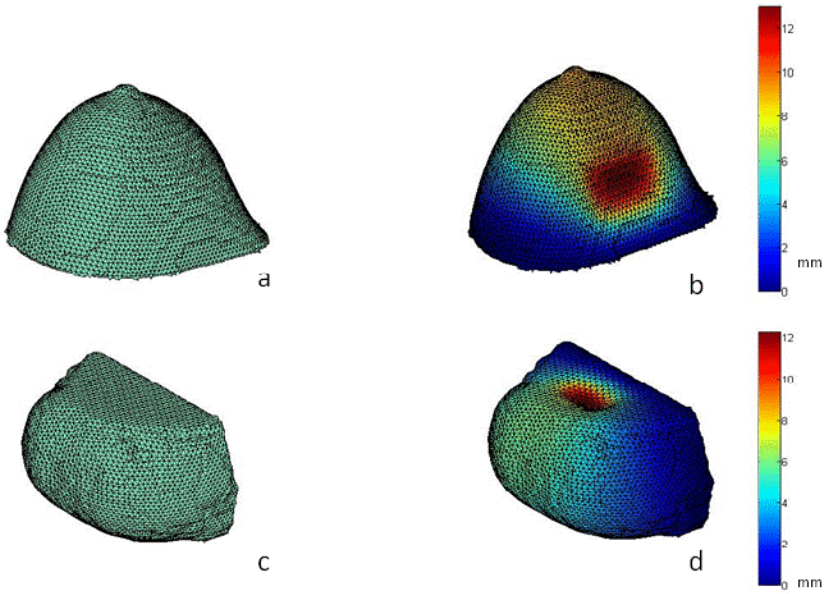

Figure 4. Source CT mesh (a) and simulated target CT mesh (b), where the colorbar refers to the magnitude of the displacement applied by the known boundary conditions to result in the target. Source MR mesh (c) and simulated target MR mesh (d) similarly shown.

The demons method was then used to register the source images to their respective target images and automatically generate boundary conditions for the source meshes. The TRE calculated from the boundary nodes was then calculated, and is visualized in Figure 5.

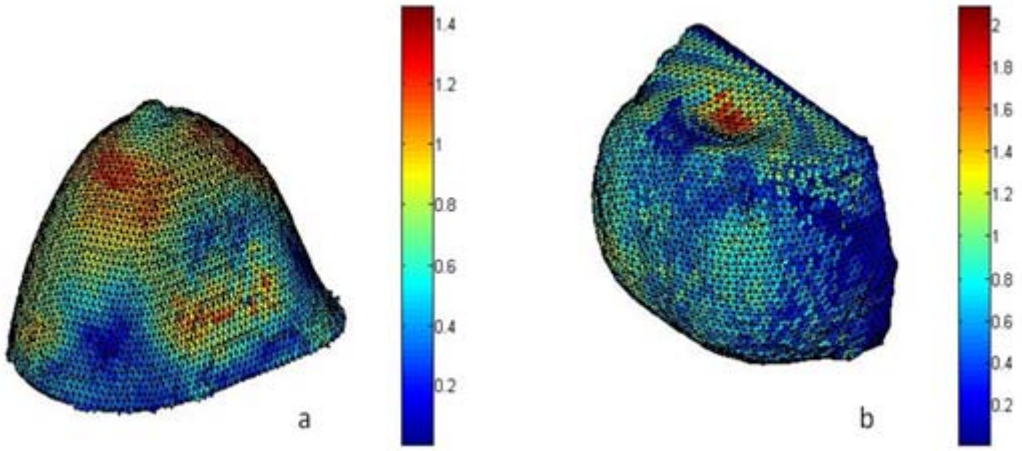

Figure 5. TRE distribution (in mm) across the surfaces of the CT mesh (a) and the MR mesh (b) for the demons-based boundary conditions compared to the known conditions.

The red surfaces of the mesh correspond to areas that experienced greater error when compared to the known boundary conditions. Averaging over all the nodes on the boundary, the CT set experienced a mean error of 0.6 mm ±0.3 mm with a maximum error of 1.5 mm, which represents an average difference of about 17% between the magnitude of the TRE vectors and the magnitudes of the known displacement vectors. The MR set experienced a mean error of 0.5 mm ± 0.3 mm with a maximum error of 1.9 mm, which represents a mean difference of about 23%. The demons-based boundary conditions were then utilized in an MIE reconstruction as described in Chapter II. The tumor-to-normal elasticity contrast calculated by the MIE algorithm was 3.63:1 for the CT set, and was 5.46:1 for the MR set. The results of the boundary condition accuracy and the resulting contrast ratios are shown in Table 1, as well as a comparison with the results of the three other boundary condition methods.

Table 1. Comparison of boundary condition mapping error and MIE reconstruction results between the four methods. The boundary error was calculated against known boundary conditions, and the MIE reconstructions were compared against the known contrast ratio of 6:1.

	Boundary Condition Mapping Error		MIE Reconstruction Results	
	CT Mean TRE (max) mm	MR Mean TRE (max) mm	CT Elasticity Contrast Ratio	MR Elasticity Contrast Ratio
TPS (40 pts.)*	0.30 (2.6) *	0.033 (0.6)*	5.66**	6.26**
Laplace*	0.53 (2.6)*	0.48 (2.5)*	5.02**	673**
Diffusion*	1.5 (8)*	0.61 (2.9)*	17.5**	348**
Demons	0.60 (1.5)	0.50 (1.9)	3.63	5.46

* (Ong, Ou et al. 2010)
**(Ou, Ong et al. 2008)

Figure 6 below illustrates the relationship between elasticity contrast ratios (tumor-to-normal) and the associated objective function values in the MIE optimization routine. The minima in the objective function space correspond to elasticity contrast values which resulted in an optimally deformed image. Shown in the figure are the objective function values of the deformations using the known boundary conditions (as the control) and the demons boundary conditions.

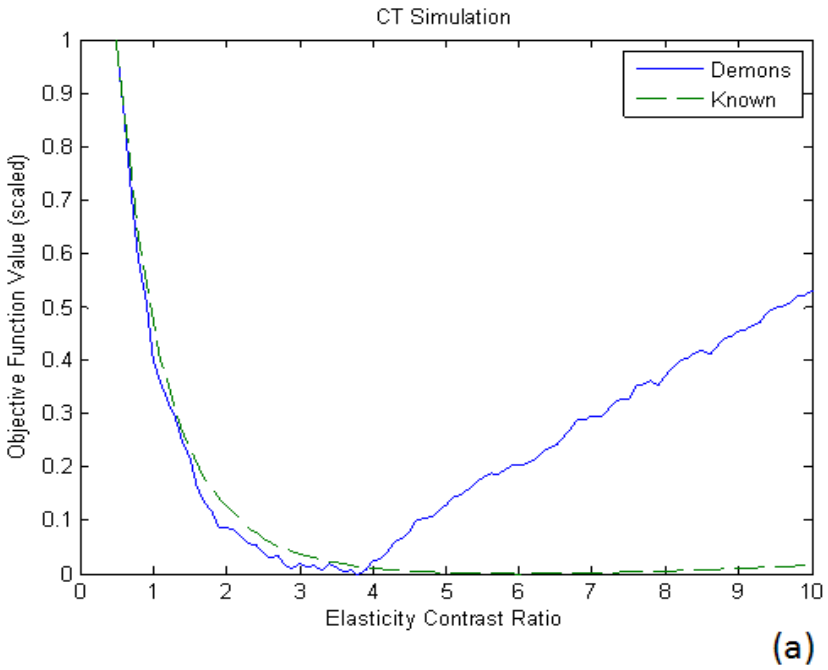

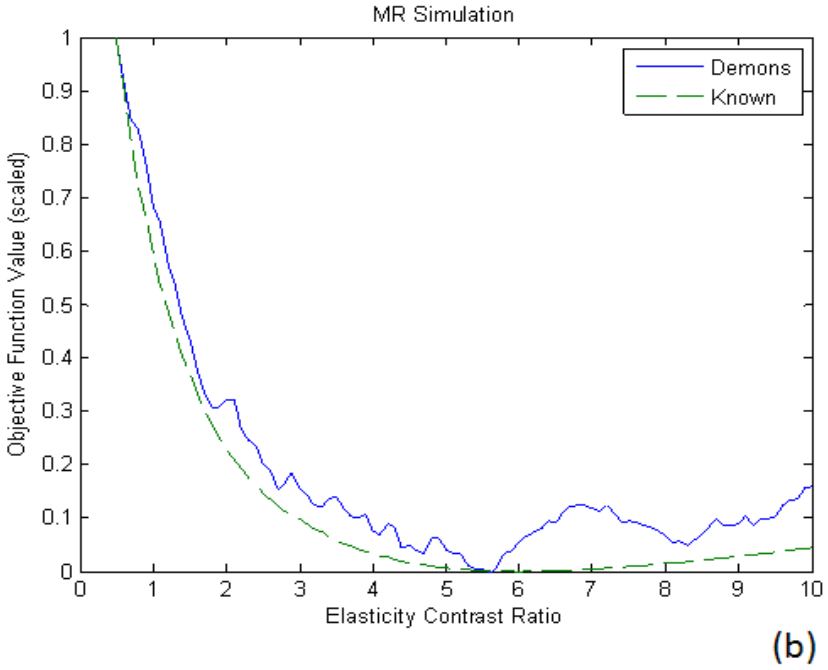

Figure 6. Objective function maps for the CT simulation (a) and the MR simulation (b). The objective function value calculated by the optimization framework is plotted on the ordinate axis against selected elasticity contrast ratios (tumor-to-normal) as affected by the boundary conditions. Shown are the objective maps of the demons case (solid lines) and the known boundary conditions as the control (dashed lines). The ordinate is scaled in both cases.

3.2 Phantom Experiment 1

CT images of Phantom 1 were acquired at no compression, 50% compression, and 100% compression and segmented from the compression chamber. Representative slices of the phantom at each deformation state are shown below in Figure 7.

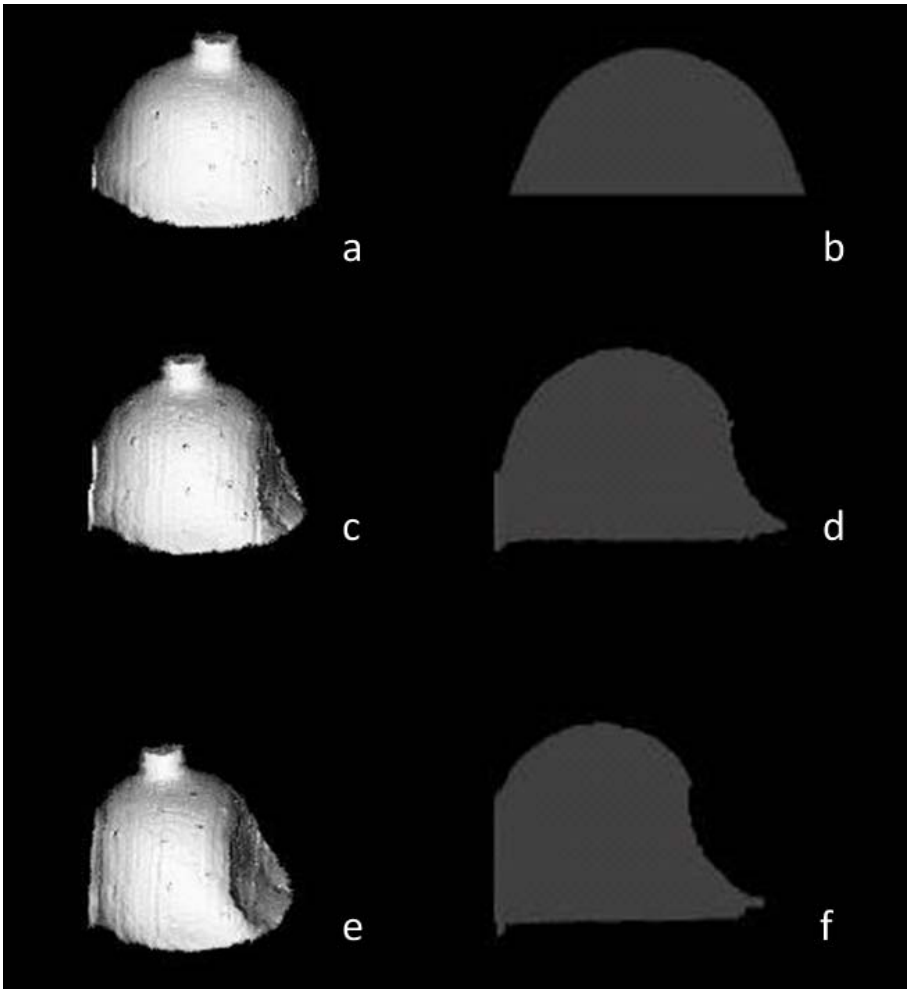

Figure 7. Surface renderings and representative slices from Phantom 1 at each state of deformation. This phantom exhibits little contrast and contains no tumor, and so was used only for testing boundary condition accuracy instead of a full MIE reconstruction. The figures in (a) and (b) display the phantom with no compression, (c) and (d) display the phantom under 50% compression, and (e) and (f) display the phantom under 100% compression.

The demons method was then used to generate Type I boundary conditions to map from the uncompressed state to the 50% state, and another set of boundary conditions to map from the uncompressed state to the 100% state. The implanted beads on the surface of the phantom were used to calculate the TRE of this surface registration in both cases. The average TRE for 50% compression when using the demons boundary conditions was approximately 3.3 mm ±1.32 mm, with a maximum TRE of about 6.1 mm. The average TRE for 100% compression was approximately 6.8 mm ±3.2 mm, which a maximum of about 14.2 mm. The Phantom 1 results are directly compared in Table 2 (see Section 3.3) to the gold standard TPS result and the results of the previous semi-automated methods, as well as to analogous results from Phantom 2 and Phantom 3.

3.3 Phantom Experiment 2

CT images of Phantom 2 and Phantom 3 were acquired and segmented from the compression chamber. The surfaces of the pre-deformed and post-deformed phantoms are displayed in Figures 8 and 9, as well as representative slices of their respective image volumes showing displacement of the tumor when subjected to the air bladder compression.

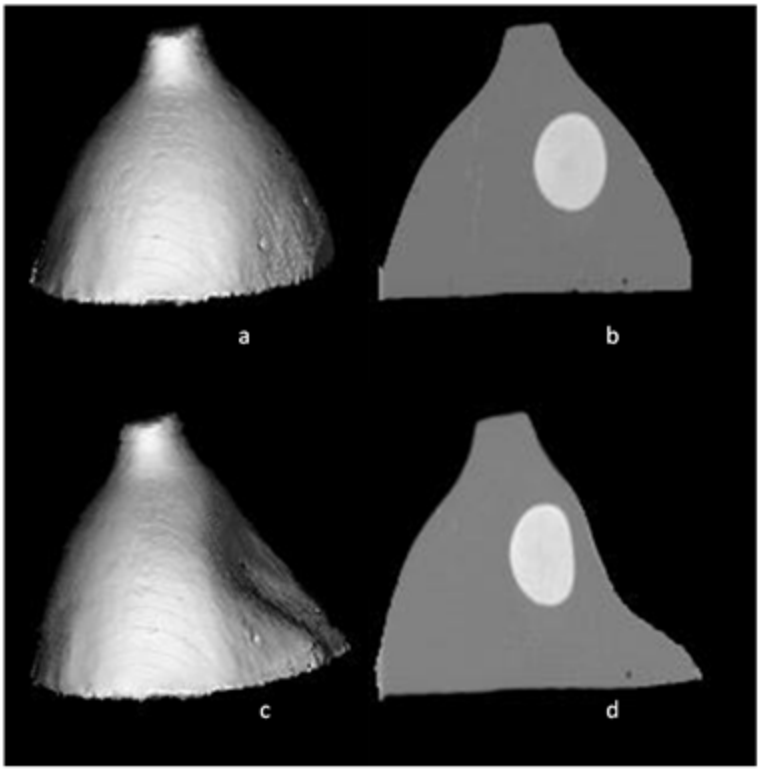

Figure 8. Surface renderings and representative slice of Phantom 2 while pre-deformed (a,b), and while under 100% bladder compression (c,d).

Figure 8 shows the embedded tumor in Phantom 2 as it was enhanced by barium sulfate to provide contrast from the bulk gel. As seen in the figure, the tumor was relatively close to the site of applied deformation, at about 12 mm from the surface. Qualitatively, the streams of barium sulfate which were distributed throughout the gel provided an increase in the image texture of these phantom images compared to the previous images of Phantom 1, which lacked this texture enhancement.

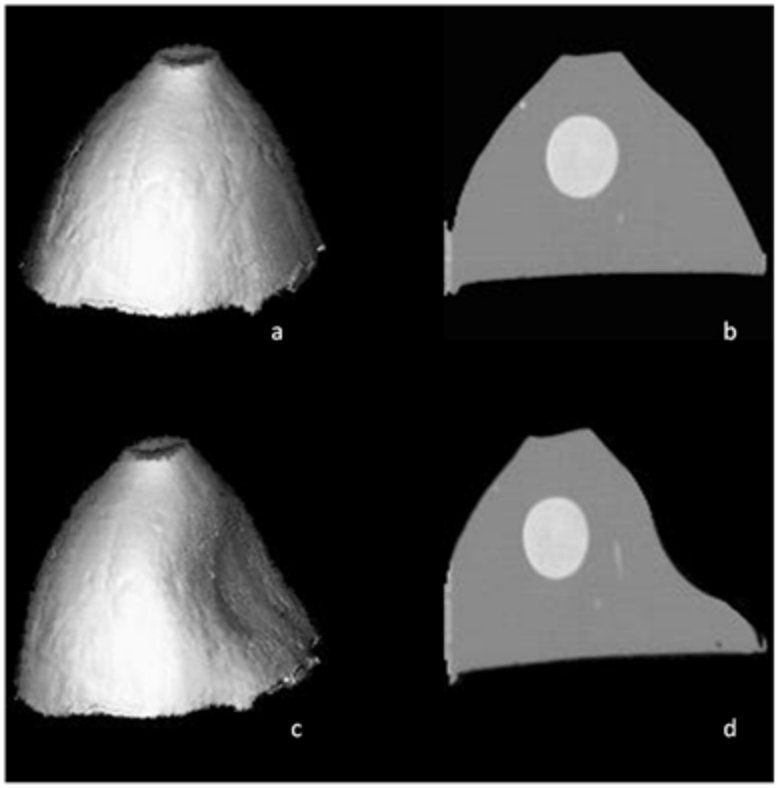

Figure 9. Surface renderings and representative slice of Phantom 3 while pre-deformed (a,b), and while under 100% bladder compression (c,d).

Figure 9 shows that the images and applied deformation for Phantom 3 were similar to those of Phantom 2. However, the tumor in this case was located further from the site of depression than in Phantom 2, at about 26 mm from the surface.

The demons method was applied to each phantom data set to acquire Type I boundary conditions for each mesh. The TRE of the demons-based conditions was then evaluated by comparing to the known point correspondence of the implanted surface beads. The average demons-based TRE for Phantom 2 was calculated to be approximately 1.6 mm ±1.0 mm, with a maximum experienced TRE of 4.9 mm. For Phantom 3, the average TRE was 1.9 mm ±1.2 mm, with a maximum experienced TRE of 4.3 mm. These values are directly compared in Table 2 to the performance of the gold standard TPS interpolation method and two previous semi-automated methods, as well as

the Phantom 1 results. As the results show that the PDE-based methods were not notably more accurate for Phantoms 2 and 3 than the TPS or demons methods, only the demons method and TPS method were used in MIE reconstructions for comparison.

Table 2. Comparison of boundary condition mapping error for Phantom 1, Phantom 2, and Phantom 3. The error was calculated against the localized positions of fiducial beads in the source and target images.

	Boundary Condition Mapping Error			
	Phantom 1		Phantom 2	Phantom 3
	50% Compression Mean TRE (max) mm	100% Compression Mean TRE (max) mm	Single Compression Mean TRE (max) mm	Single Compression Mean TRE (max) mm
TPS	1.1 (3.4)*	1.7 (5.1)*	1.4 (7.08)**	1.24 (4.9)**
Laplace	3.4 (8.6)*	6.3 (15.3)*	4.22 (7.26)	2.24 (4.74)
Diffusion	2.7 (6.9)*	5.7 (13.6)*	4.11 (6.57)	2.35 (6.36)
Demons	3.3 (6.1)	6.8 (14.2)	1.55 (4.92)	1.85 (4.34)

*(Ong, Ou et al. 2010)
**Based on work in (Ou 2008)

The material testing data resulted in an average contrast ratio of 4.10:1 for the gels. The demons-based boundary conditions were then used in an MIE reconstruction for each phantom. The tumor-to-normal elasticity contrast for Phantom 2 was calculated by the MIE algorithm to be 4.70:1. The elasticity contrast for Phantom 3 was calculated to be 2.46:1. In Table 3 below, these values are compared to the contrast ratios that were calculated by MIE using the gold standard TPS boundary conditions, and to the material testing data as validation for the accuracy of the MIE method.

Table 3. Comparison of the MIE-reconstructed elasticity contrast ratios for Phantom 2 and Phantom 3 when using TPS and demons boundary conditions, as well as the mean contrast observed via material testing of the gels.

	Phantom 2 Reconstructed Contrast Ratio	Phantom 3 Reconstructed Contrast Ratio	Material Tester Contrast Ratio*
TPS*	3.81	3.06	4.10
Demons	4.70	2.46	

*(Ou, Ong et al. 2008)

Figure 10 below illustrates the relationship between elasticity contrast ratios (tumor-to-normal) and the associated objective function values in the MIE optimization routine. Shown in the figure are the objective function values of the deformations using the TPS boundary conditions (as the control) and the demons boundary conditions.

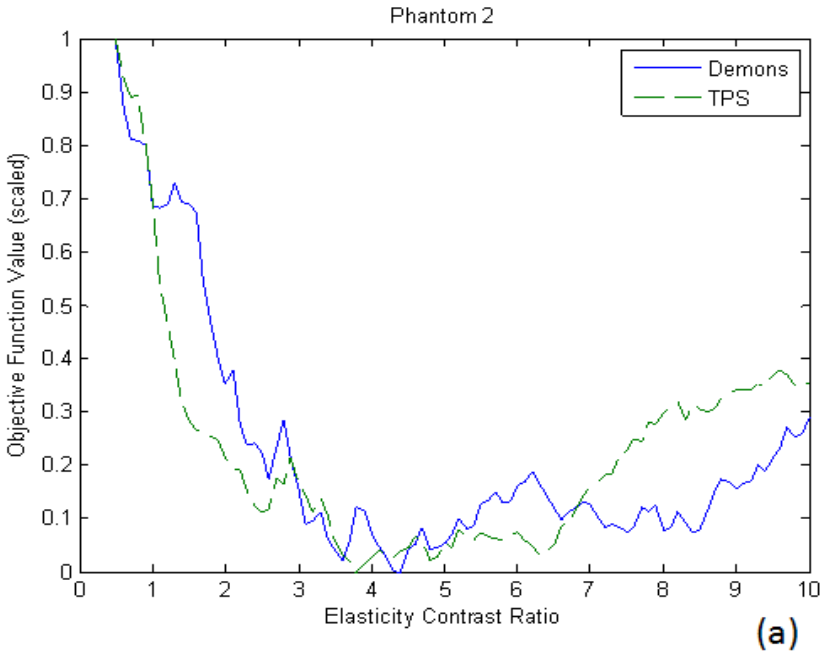

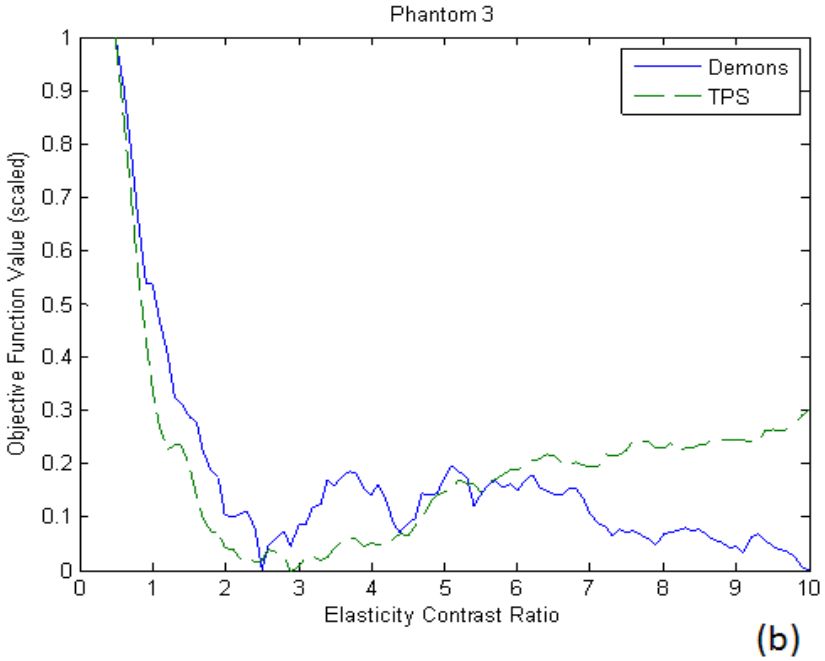

Figure 10. Objective function maps for Phantom 2 (a) and the Phantom 3 (b). The objective function value calculated by the optimization framework is plotted on the ordinate axis against selected elasticity contrast ratios (tumor-to-normal) as affected by the boundary conditions. Shown are the objective maps of the demons case (solid lines) and the TPS boundary conditions as the control (dashed lines). The ordinate is scaled in both cases.

CHAPTER IV

DISCUSSION

4.1 Simulations

The demons-based boundary conditions resulted in deformed meshes which were qualitatively very close in appearance to the known target meshes for both the CT and MR data sets. Quantitatively, the average difference between the demons conditions and the known conditions was about 20% for both sets, which was an encouraging indication of the ability of the demons methods to automatically provide boundary conditions which would have adequate accuracy for use in MIE. In Figure 5, it can be seen that the largest errors were spread across the regions of high curvature around the tip of the breast and in the dip of the artificial depression for the CT set, while in the MR set the errors were mostly localized to the depression area.

The accuracy of the demons-based boundary conditions for the CT simulation was compared to the results of past methods in Table 1 (see Section 3.1). Unsurprisingly, the TPS method remained the most accurate of the four methods when considering the average boundary condition error. The demons method performed about as well as the Laplace method, and clearly outperformed the diffusion method in terms of the average error. However, the demons method performed favorably compared to all of the other methods in terms of maximum TRE, as its maximum error was well below those of the other methods.

A similar comparison of these boundary condition methods applied to the MR simulation was also shown in Table 1. The TPS interpolation again resulted in the most

accurately generated boundary conditions of the four methods. In terms of average surface TRE, the demons method was also again comparable to the Laplace method, as well as the diffusion method in this case. However, with the exception of the TPS method, the demons boundary conditions once again compared favorably against the other methods in terms of the maximum error experienced on the boundary.

The results of the boundary condition accuracy experiment were encouraging and indicated that demons-based boundary conditions were a feasible solution to the MIE boundary condition problem. The results of the MIE reconstruction for the CT and MR sets were shown in Table 1 and compared to the results of reconstructions which utilized boundary conditions generated from the other three methods. Unsurprisingly, the table shows that the TPS boundary conditions, which were the most accurate of the four, resulted in elasticity contrast ratios for both sets that were closer to the known ratio of 6:1 than any of the other boundary conditions. For the application of the demons registration-based boundary conditions to the CT data set, the elasticity reconstruction with spatial *a priori* knowledge of the tumor successfully converged to a contrast ratio of 3.63:1. Similarly, the MR data resulted in a contrast ratio of 5.46:1. Compared to the known designated material contrast of 6:1, there is clearly a discrepancy in these reconstruction behaviors that needs to be investigated. The difference, particularly between the different modalities of input data, is likely due to a combination of factors including mesh geometry and image quality. In addition, the distance of the tumor from the area of greatest displacement likely affects the accuracy of the reconstruction since the displacements of nodes are expected to decrease the further they are located away from the depression. These simulations did not investigate the effect of tumor distance on the

reconstruction. Interestingly, the diffusion method resulted in a much higher contrast ratio for the CT set than the demons method, while the Laplace method resulted in a contrast ratio that was closer to 6:1 but was an underestimation rather than an overestimation of the true value. The ability of the demons-based conditions to provide a contrast that was more accurate than the diffusion method for the CT simulation was encouraging. Even more suggestive was the behavior of the MR reconstruction. The Laplace and diffusion boundary conditions introduced instabilities into the MIE algorithm, which resulted in contrast estimates that were unreasonably higher than the true value. The demons-based conditions allowed the algorithm to provide a contrast estimate which was closer to the known value.

It is also interesting to note the effect of the demons boundary conditions on the optimization, as shown in Figure 6. Introducing the inexact demons boundary conditions to the model had a noticeable effect by shifting the minimum objective function value to a different optimal elastic contrast ratio for both the CT and the MR simulation. The shift was much more pronounced for the CT simulation, for which the new optimal objective function value corresponded to a contrast ratio of about 3.80:1 instead of 6:1 as predicted by the known boundary conditions. Additionally, the convexity of the function was altered significantly, with very little variation in the objective function for contrast ratios in the immediate vicinity of the global minimum. The MR simulation also experienced a shift in the optimal objective function when demons boundary conditions were used instead of the known conditions, with a new optimal contrast of about 5.50:1. This represented only a slight decrease from the desired 6:1 prediction. The objective function values arise from the image similarity metric, which again suggests that the difference in

objective maps between the two simulations is influenced by the image texture characteristics. It is also clear that the addition of inaccuracies within the boundary conditions due to the registration process alters the nature of the objective function by injecting local minima and undesirable variations. It is evident that some sort of iterative filtering approach may be necessary to ensure that global minima are found.

4.2 Phantom Experiment 1

While the efficacy of the automated demons method was shown by the simulations to be comparable to the semi-automated Laplace method and somewhat better than the diffusion method, the simulations were in several ways performed under optimal conditions. The image volumes qualitatively had a great deal of heterogeneity and texture on which the demons registration could act, and with which the MIE optimization routine could use to help accurately update material property assignments. There was also an absolute truth with which to compare, in the form of known boundary conditions. The first phantom experiment sought to provide additional challenge to the demons method in its ability to generate reasonably accurate boundary conditions.

The results of the demons registration were compared to the results of the three other methods in Table 2 (see Section 3.3) for the two compression states applied to Phantom 1. Interestingly, the table shows that the demons algorithm performed about as well in relation to the other PDE methods as it did in the simulation experiment. What is interesting about this is that Phantom 1 had very little image heterogeneity and would indicate that with a lack of image intensity contrast that the demons-based registration is at least no worse than that achieved by the PDE methods. The gold standard TPS method

gave the lowest error. As seen in Table 2, the errors given by all of the methods increased when a larger deformation was applied to Phantom 1. The demons boundary conditions became slightly worse in relation to the other methods at the increased level of compression, which suggests that the number of iterations used by the demons algorithm may need to be increased to accommodate larger differences between pre- and post-deformation images, or that the algorithm may be somewhat more sensitive to the lack of image intensity heterogeneity.

It is also interesting to note that in moving from simulation data to "real-world" phantom data, the errors experienced by all four of the methods increased significantly. The Phantom 1 image data was different from the simulation data in several key respects. For example, the target image volume of Phantom 1 represents a completely new acquisition, whereas in the simulation work post-deformed image sets were generated from the pre-deformed set. This discrepancy in target image acquisition introduces some uncertainty to the determination of source-to-target correspondence. Another major change from the simulation experiment was the markedly smaller presence of texture in the images due to the homogeneity of the gel. More specifically, it is interesting to note the change in TRE performance among the Phantom 1, Phantoms 2&3, and simulation results which are listed respectively in terms of increasing image texture. Qualitatively observing the results across Tables 1 and 2, the trend of decreasing TRE with increasing texture for the demons-based approach can be observed.

4.3 Phantom Experiment 2

It was shown in the first phantom experiment that the demons method could produce reasonably accurate boundary conditions compared to the semi-automated Laplace and diffusion methods. The second phantom experiment introduced another set of real-world data, but the images from this experiment had more texture in the form of barium sulfate as a contrast agent, which was intended to allow the demons registration to provide more accurate boundary conditions as needed by the MIE algorithm. In addition, the presence of the stiff tumor allowed for a test of the MIE algorithm's ability to distinguish elasticity contrast in a phantom while using demons-based boundary conditions. This experiment was thus the first in which demons-based boundary conditions were used in an MIE reconstruction for which the true boundary conditions were not absolutely known.

The surface errors calculated from the fiducial point correspondence for the TPS, Laplace, diffusion and demons methods were compared in Table 2 (see Section 3.3) for Phantom 2 and Phantom 3. Unsurprisingly, the TPS method performed better with respect to mean accuracy. Notably, the maximum error experienced by the demons method was less than that of the TPS method, which was similar to the result of the CT simulation study. The two PDE-based methods presented error which was similar in scope to their Phantom 1 results. Overall, the demons method performed considerably better on these two phantom sets than it did on Phantom 1, and notably outperformed the Laplacian and diffusion methods. This is most likely due to the increase in image texture which can be qualitatively observed from visual inspection of the images. Given that

clinical images tend to have even more image texture and geometric heterogeneity than found in these phantom images, further investigation into the efficacy of the demons method seems merited.

The utilization of the demons boundary conditions in MIE reconstructions successfully resulted in realistic tumor-to-normal modulus contrast ratios for both phantoms. Due to the observation that the demons method resulted in boundary conditions with comparable (and sometimes superior) accuracy to the Laplace and diffusion methods, only the TPS and demons boundary conditions were utilized in these reconstructions. The results for the TPS- and demons-based MIE reconstructions were compared to each other in Table 3 (see Section 3.3) as well as to the material tester results. As the table shows, the elasticity contrast ratios for each phantom when using TPS boundary conditions were reconstructed to values that were within 14-40% of the material testing data average. The reconstructions using demons boundary conditions resulted in contrast ratios which were very similar to those of the TPS-based reconstructions, with only a slight drop in contrast. This suggests that the demons boundary conditions were sufficiently accurate for the MIE algorithm to provide a reasonable estimate of the actual gel contrast.

It is also interesting to note the effect of the demons boundary conditions on the optimization, as shown in Figure 10. Compared to the control TPS boundary conditions, the demons conditions had a noticeable effect by shifting the minimum objective function value to a different optimal elastic contrast ratio for both phantoms. Additionally, the convexity of the function was altered slightly for each. Interestingly, the global minimum of the Phantom 2 objective function was located at an approximate contrast ratio of

4.20:1, which was more similar to the material testing average of 4.10:1 than the case in which TPS boundary conditions were used. The actual contrast ratio to which the MIE reconstruction converged was 4.70:1, which was located on the slope of a local minimum. This behavior was most likely a result of the regularization parameters used in the Levenberg-Marquardt optimization. In the case of Phantom 3, the global minimum was about 2.50:1, which was the approximate value to which the algorithm converged. In this case, the global minimum decreased slightly when using demons instead of TPS conditions.

Observations of Figures 6 and 10 indicate the change in algorithm performance with respect to simulation and physical data. While the nature of a simulation-to-real transition may be responsible for the increased error in reconstruction, there are several other likely factors involved. Over-constraint of the problem is a possible candidate with the incorporation of the spatial prior. The MIE method works by sampling similarity regionally, i.e. the method breaks up evaluation into many similarity zones (usually over 100) distributed spatially over the domain. The method tries to improve the similarity among all the zones with the use of only two parameters in this case (the elasticity of the background and tumor). This level of constraint within this type of problem can lead to this type of oscillatory behavior. Another possible reason is the inaccuracy in boundary condition determination due to the dramatic difference in image heterogeneity between simulation and real data. This is supported by the change in TRE. Related to this, it is interesting to note the difference between CT and MR reconstruction for the simulation work associated with Figure 6 and in light of Table 1. The first observation can be made by comparing the control objective function map across CT and MR simulation sets in

Figure 6. Both simulation sets had a contrast ratio of 6:1, with the only difference being the level of intensity heterogeneity, and potential different breast/tumor geometries/locations. It can be observed that the CT control had a shallower minimum which may affect the reconstruction. When adding to this observation the objective function maps associated with the demon-based boundary condition it would seem at first glance that the CT reconstruction may perform better due to its convexity; but when observing how the minimum has been shifted, and in light of the shape of the control that has no error in boundary conditions, it can be seen that in fact the MR demons-based objective function maps more closely to its control which is reflected in the elasticity contrast ratio.

CHAPTER V

CONCLUSION

The simulations and both phantom experiments conducted in this work indicate that while TPS interpolation remains the most accurate method used thus far in MIE for generating boundary conditions, the demons method shows promise in situations where fiducial point correspondence data may not be available. In addition, when transitioning from simulation to real data, the discrepancy in performance between TPS and the demons-based boundary condition mapping becomes less (at least in cases where image intensity contrast within the domain is available). Furthermore, while the higher accuracy of the TPS method is desirable, the much higher level of manual user interaction and numerous fiducials needed for the method make clear the desire for alternative methods of boundary condition generation. The previously studied PDE-based methods represented steps toward automation of the boundary condition step, but still required a moderate level of user interaction in manually designating boundary conditions to various portions of the mesh. The demons method proposed represents a fully automated approach.

While the results are encouraging, the challenge of predicting (prior to workflow initiation) how well a pre-post deformation image set will fare prior to execution of the demons registration and MIE optimization routine still remains. Since the demons registration algorithm possesses diffusive behavior based upon intensity contours as described by Thirion (1998), it is obvious that the images require a certain level of texture

and intensity heterogeneity in order to provide these membranes a meaningful registration. This is one of the likely causes of the varying performance of the demons method in generating accurate boundary conditions among the experiments presented in this work. The MIE algorithm has similar requirements in order to correctly optimize image similarity at each update with respect to realistic material properties in the model. Development of a feasibility metric which can predict the success of applying the MIE algorithm to a given image set is a needed next step for the project.

In addition to a threshold criterion to evaluate the potential for a successful reconstruction, the need to generate more realistic phantoms with controllable stiffness properties is also necessary. The breast has a complex image signature even within CT and the reproduction of those patterns coupled with controllable elasticity properties is very challenging. While obstacles remain, the results presented here demonstrate the potential of treating elastographic reconstructions using non-rigid image registration approaches and that the possibility of full automation is also within reach.

REFERENCES

ACS (2009). Cancer Facts & Figures 2009. Atlanta, American Cancer Society.

Bilgen, M. (1999). "Target detectability in acoustic elastography." Ieee Transactions on Ultrasonics Ferroelectrics and Frequency Control **46**(5): 1128-1133.

Burns-Cox, N., N. C. Avery, et al. (2001). "Changes in collagen metabolism in prostate cancer: a host response that may alter progression." J Urol **166**(5): 1698-701.

Doyley, M. M., P. M. Meaney, et al. (2000). "Evaluation of an iterative reconstruction method for quantitative elastography." Phys Med Biol **45**(6): 1521-40.

Goshtasby, A. (1988). "Registration of Images with Geometric Distortions." Ieee Transactions on Geoscience and Remote Sensing **26**(1): 60-64.

Guo, Y., R. Sivaramakrishna, et al. (2006). "Breast image registration techniques: a survey." Med Biol Eng Comput **44**(1-2): 15-26.

Ibanez, L., W. Schroeder, et al. (2005). The ITK Software Guide, Kitware, Inc.

Keith, L. G., J. J. Oleszczuk, et al. (2002). "Are mammography and palpation sufficient for breast cancer screening? A dissenting opinion." J Womens Health Gend Based Med **11**(1): 17-25.

Krouskop, T. A., T. M. Wheeler, et al. (1998). "Elastic moduli of breast and prostate tissues under compression." Ultrason Imaging **20**(4): 260-74.

Lee, H., K. L. Sodek, et al. (2007). "Phagocytosis of collagen by fibroblasts and invasive cancer cells is mediated by MT1-MMP." Biochem Soc Trans **35**(Pt 4): 704-6.

Michaelson, J. S., M. Silverstein, et al. (2002). "Predicting the survival of patients with breast carcinoma using tumor size." Cancer **95**(4): 713-23.

Miga, M. I. (2003). "A new approach to elastography using mutual information and finite elements." Phys Med Biol **48**(4): 467-80.

Miga, M. I., M. P. Rothney, et al. (2005). "Modality independent elastography (MIE): potential applications in dermoscopy." Med Phys **32**(5): 1308-20.

Muthupillai, R., D. J. Lomas, et al. (1995). "Magnetic resonance elastography by direct visualization of propagating acoustic strain waves." Science **269**(5232): 1854-7.

Ong, R. E., J. J. Ou, et al. (2010). "Non-rigid registration of breast surfaces using the laplace and diffusion equations." Biomed Eng Online **9**(1): 8.

Ophir, J., I. Cespedes, et al. (1991). "Elastography: a quantitative method for imaging the elasticity of biological tissues." Ultrason Imaging **13**(2): 111-34.

Ou, J. J. (2008). Development of modality-independent elastography as a method of breast cancer detection**:** xiv, 169 p. (1 file).

Ou, J. J., R. E. Ong, et al. (2008). "Evaluation of 3D modality-independent elastography for breast imaging: a simulation study." Phys Med Biol **53**(1): 147-63.

Papademetris, X., A. J. Sinusas, et al. (2002). "Estimation of 3-D left ventricular deformation from medical images using biomechanical models." IEEE Trans Med Imaging **21**(7): 786-800.

Sullivan, J. M., G. Charron, et al. (1997). "A three-dimensional mesh generator for arbitrary multiple material domains." Finite Elements in Analysis and Design **25**(3-4): 219-241.

Thirion, J. P. (1998). "Image matching as a diffusion process: an analogy with Maxwell's demons." Med Image Anal **2**(3): 243-60.

Warwick, J., L. Tabar, et al. (2004). "Time-dependent effects on survival in breast carcinoma: results of 20 years of follow-up from the Swedish Two-County Study." Cancer **100**(7): 1331-6.

Yoo, T. S., M. J. Ackerman, et al. (2002). "Engineering and algorithm design for an image processing Api: a technical report on ITK--the Insight Toolkit." Stud Health Technol Inform **85**: 586-92.